Rotating fins in phase change materials for cyclable high-power density latent thermal energy storage

Original
Rotating fins in phase change materials for cyclable high-power density latent thermal energy storage / Agegnehu, B., Ribezzo, A., Bottega, A., Morciano, M., Fasano, M., Chiavazzo, E.. - In: JOURNAL OF ENERGY STORAGE. - ISSN 2352-152X. - ELETTRONICO. - 160:(2026). [10.1016/j.est.2026.121877]

Publisher:
Elsevier

Published
DOI:10.1016/j.est.2026.121877

Journal of Energy Storage 160 (2026) 121877

Contents lists available at ScienceDirect

Journal of Energy Storage

journal homepage: www.elsevier.com/locate/est

Research papers

Rotating fins in phase change materials for cyclable high-power density latent thermal energy storage

Biruk Agegnehu, Alessandro Ribezzo, Andrea Bottega, Matteo Morciano, Matteo Fasano, Eliodoro Chiavazzo *

Department of Energy, Politecnico di Torino, Corso Duca degli Abruzzi 24, 10129 Torino, Italy

ARTICLE INFO

Keywords:
Phase change material
Thermal energy storage
High power density
Rotating fins
Dynamic PCM

ABSTRACT

This study proposes a novel dynamic thermal enhancement technique for latent thermal energy storage based on a rotating helical screw fin inspired by Archimedean geometry. The system integrates mechanical scraping and convective mixing into a single mechanism that can effectively operate during both melting and solidification phases of phase change materials (PCMs). In this study, experimental results validate the concept for the solidification process, showing improved heat transfer performance and power density compared to a baseline configuration without fins. Particularly, the introduction of this rotating helical screw fin led to reductions of 46% and 50% in solidification times for $\Delta T = 20\,^{\circ}\mathrm{C}$ and $\Delta T = 10\,^{\circ}\mathrm{C}$, respectively. This study further highlights the potential of mechanical aids to enhance thermal transfer in latent thermal energy storage, thus possibly opening new pathways for efficient PCM-based thermal management.

1. Introduction

Phase change materials (PCMs) have attracted significant interest in thermal energy storage (TES) and thermal management applications over the past couple of decades, driven by the global shift toward clean energy solutions [1,2]. Due to their high latent heat and narrow phase-transition temperature range, PCMs hold promise for a wide range of applications, including electronic thermal management [3,4], textiles [5], and buildings [6]. PCMs are generally classified into three major categories based on their material composition: organic, inorganic, and eutectic [7].

Similar to other energy storage technologies, the performance of PCM-based TES systems is predominantly evaluated based on two key figures of merit: energy density and power density. Although the nominal energy density is governed by the latent heat capacity of the PCM, the power density is primarily constrained by the inherent low thermal conductivity of most PCMs, particularly organic ones. These materials, despite offering high latent heat, exhibit poor heat transfer characteristics [8]. Addressing this thermal bottleneck has become a central theme in PCM research [9]. A wide range of strategies have been proposed to improve the effective thermal conductivity of PCMs, including the integration of highly conductive static structures [10–12], nanofillers [12–14], and advanced encapsulation techniques that promote efficient heat exchange [15,16]. While many of these thermal enhancement strategies have demonstrated success in improving heat transfer performance, they generally compromise the energy storage capacity of the system to a non-negligible extent, by decreasing the available volume for the PCM. Moreover, a critical yet often overlooked phenomenon is the migration of the solid–liquid interface–the dynamic front at which latent heat exchange occurs–moving from the heat source. This shift leads to the accumulation of low-conductivity liquid and solid PCM between the heat source and the phase front, thereby exacerbating thermal resistance and diminishing the system's overall power density in time.

Heat transfer enhancement strategies in PCM-based TES systems are broadly categorized into two main approaches: passive and active [17,18]. Passive techniques, such as adding extended metal fins, using composite PCMs, dispersing high thermal conductivity nanoparticles, and encapsulating the PCM, enhance thermal performance without external energy input. Conversely, active enhancement strategies rely on external energy inputs to improve the effective power density of the PCM. These include vibration [19–21], jet impingement [22,23], fluid injection [24,25], external fields [26–28], mechanical aids and pressure [29–32]. An overview of these active techniques is available in the work authored by Kyle et al. [33].

While mechanical aids have been extensively studied for enhancing the melting phase, their application to improve the solidification process of PCMs remains less explored. This is a critical gap, as solidification is widely recognized as the primary bottleneck limiting the

---

* Corresponding author.
E-mail address: eliodoro.chiavazzo@polito.it (E. Chiavazzo).

https://doi.org/10.1016/j.est.2026.121877
Received 16 September 2025; Received in revised form 17 February 2026; Accepted 27 March 2026

Nomenclature

$A(f)$	Porosity damping function [-]
c_p	Specific heat capacity [J/(kg K)]
C	Mushy zone constant [kg m^{-3} s^{-1}]
D	Diameter [m]
f	Liquid fraction [-]
$\mathbf{F}_g$	Volume buoyancy force [N/m^3]
$\mathbf{F}_u$	Velocity damping force [N/m^3]
$\mathbf{g}$	Gravitational acceleration [m/s^2]
H	Height [m]
$\mathbf{K}$	Viscous stress tensor [Pa]
k	Thermal conductivity [W/(m K)]
L	Latent heat [J/kg]
p	Pressure [Pa]
P	Penalization term [-]
R_{th}	Thermal resistance [K m^2/W]
s	Phase transition front position
S_h	Latent heat source [W/m^3]
t	Time [s]
t_{round}	Time needed to obtain a complete rotation [s]
T	Temperature [°C]
ΔT	Temperature difference between the cooling surface and the solidification temperature [°C]
ΔT_m	Half of the mushy zone [°C]
T_f	Solidification temperature [°C]
T_{initial}	Initial temperature [°C]
T_{pc}	Phase change temperature [°C]
$\mathbf{v}$	Velocity vector [m/s]
x, y	Coordinates [m]
α_s	Thermal diffusivity in solid phase [m^2/s]
ϵ	Small numerical constant [-]
λ	Parameter of the Neumann solution to the Stefan problem [-]
μ	Dynamic viscosity [Pa s]
ρ	Density [kg/m^3]
$_l$	Subscript for liquid
$_s$	Subscript for solid
HTF	Heat transfer fluid
PCM	Phase change material
TES	Thermal energy storage

power density of latent thermal energy storage systems. Mechanical enhancement strategies typically involve the rotation of the storage enclosure or the agitation of the PCM, thereby promoting forced convection and improving thermal performance. In this context, Huang et al. [34] conducted a numerical investigation into the solidification behavior of a triplex-tube TES system subjected to rotational motion. The study examined the heat release characteristics duration under varying rotational speeds. Notably, the results revealed that at a rotational speed of 1 RPM, the solidification time was reduced by 83.85% compared to the stationary case, while the power density increased by a factor of 4.98. A further increase in the rotational speed consistently led to reduced solidification times and larger heat transfer rates, as the rotationally-induced internal flow facilitated a more uniform temperature distribution within the PCM during solidification. Soltani et al. [35,36] investigated the synergistic effect of a combination of fins, nanoparticles, and rotational speed on the charging and discharging heat transfer rates of horizontal TES. Four different configurations with 0, 4, 8, and 16 radial copper fins, combined with rotational speeds of 0.1, 0.5, and 1 RPM, were studied. Their results showed that the greatest improvement was obtained with four fins and 1 RPM, resulting in 73.13% and 83.21% reductions in the melting and solidification times of pure n-eicosane PCM, respectively. In the subsequent study [36], they investigated the combined effect of Cu nanoparticles concentration, fin number, and rotation on charging and discharging times of a n-eicosane PCM. Various numbers of copper fins, volume fractions of copper nanoparticles, and rotational speeds were assessed, by obtaining maximum values of 78.49% and 76.88% reductions in charging and discharging times for the case with 8 fins, 0.5 RPM, and 0.05 volume fraction of copper nanoparticles. The enhancement of heat transfer performances obtained by means of the introduction of rotation motion was reported by various numerical [37–39] and experimental [40–42] studies.

A mechanical aid that has been used as a heat transfer enhancer technique for solidification (discharging) process purposes is mechanical scraping. During solidification, solid PCM begins to form starting from the heat transfer surfaces, thus forming a low thermally conductive layer which acts as an insulator between the molten PCM and the heat transfer surface. Moreover, the thickness of this layer grows during the solidification process. In this context, mechanical scraping techniques are used to remove this solid PCM from the heat transfer surfaces and reduce the thermal resistance between the heat transfer fluid (HTF) and the solidification front. Maruoka et al. [43] introduced a new technique in which a fixed blade within a shell-and-tube latent thermal energy storage system is used to scrape the solid PCM from a rotating HTF surface cylinder pipe. This study demonstrated that the heat release rate was accelerated compared to the non-rotating configuration, with an overall heat transfer coefficient that reached more than 2000 W/m^2 K at 500 RPM. Egea et al. [44] experimentally studied a cylindrical TES system with the HTF surrounding the PCM container. The effect of three different rotational speeds (3, 5, and 7.5 RPM) of three different sets of rotating blades attached to the inner pipe were tested for scraping the PCM off the outer wall of the container. A 2–3 times larger heat release rate was obtained, regardless of the rotational speed. In another study by Tombrink et al. [45], mechanical scraping methods were experimentally investigated in a horizontal rotating drum PCM-based heat exchanger with a fixed scraper that continuously removed the solid PCM layer. Their results show a consistent heat transfer, which is increasing for higher rotational speeds. Further numerical studies [46,47] showed an 8% deviation in the transient heat transfer rate from the experimental values. Also, an optimization of the system for practical applications in steam generation and co-generation of electricity was performed.

As reported in the studies mentioned above, mechanical scraping of the heat transfer surface significantly enhances the solidification rate and overall heat transfer, thus increasing the power density of the TES systems. However, existing designs often involve mechanical complexity, lack versatility for dual-phase operation, and are predominantly restricted to tube-in-tube heat exchanger configurations. Notably, the potential to apply scraping techniques during both solidification (discharge) and melting (charge) phases remains underexplored. Furthermore, their integration into more compact and versatile heat exchanger geometries such as shell-and-tube designs has yet to be fully investigated [48].

In this context, the potential of integrating mechanical scraping and convective mixing into a single, compact, and reversible mechanism remains largely unexplored, particularly for heat exchanger configurations relevant to practical TES applications. Existing solutions are predominantly restricted to dedicated laboratory setups and have limited adaptability to conventional heat exchanger architectures such as shell-and-tube designs.

In this study, we propose and experimentally evaluate a novel dynamic scraping mechanism based on a rotating helical screw fin, inspired by Archimedean screw geometry. The concept integrates a helically finned insert that rotates concentrically around the HTF pipe and is surrounded by a PCM storage unit. By adopting this configuration in the experimental tests of a solidification process, a continuous removal of the solidified PCM layer from the heat exchanger surface is obtained, along with forced convective mixing in the liquid phase. The proposed solution addresses three critical challenges in TES systems: (i) enhancement of heat transfer area via extended metallic fins, (ii) agitation-induced promotion of convection within the liquid PCM, and (iii) mechanical removal of low-conductivity solid PCM to reduce thermal resistance at the heat transfer interface. The system has been experimentally validated during the solidification process to establish proof of concept and compared against (i) the baseline case consisting of bulk PCM, and (ii) the case with static fins. Moreover, numerical counterparts of the experiments have been performed to gain insight into the three configurations. CFD simulations of the baseline and static fins case have been carried out and validated against the experimental results. The dynamic configuration (namely, the rotating helical fins) was investigated numerically using an approximate yet accurate analytical method to develop a conceptual model of the underlying mechanisms. Finally, the simplified numerical procedure was employed to perform a preliminary sensitivity analysis with respect to the rotational speed of the helical screw.

This article is structured as follows: Section 2 presents the conceptual design in detail; Section 3 describes the experimental setup and methodology; Section 4 discusses the results, and conclusions and future research directions are drawn in Section 5.

2. Concept

In a classical PCM solidification process, the solid–liquid interface moves away from the cold surface as the PCM releases its latent heat. As schematically shown in Fig. 1(A), this front progresses over time, forming a thick solid PCM layer in the proximity of the cold source. This solidified layer acts as a thermal insulating barrier between the liquid PCM and the heat transfer surface, due to the inherently low thermal conductivity of most PCMs. This increasing thermal resistance (see Fig. 1(B)) reduces the heat flux, power density, and overall performance of the TES system.

In such conventional configuration, the dynamical evolution of the solidification front can be conveniently described by the popular Stefan problem:

$$k_s \left.\frac{\partial T_s}{\partial x}\right|_{x=s(t)} - k_l \left.\frac{\partial T_l}{\partial x}\right|_{x=s(t)} = \rho_s L \frac{\partial s}{\partial t}. \tag{1}$$

Here, the thermal resistance during the solidification process can be described as:

$$R_{\mathrm{th}}(t) = \frac{s(t)}{k_s} = \sqrt{\frac{2(T_f - T_s)t}{\rho L k_s}} \propto \sqrt{t}, \tag{2}$$

where k_s and k_l are the thermal conductivities of the solid and liquid phases of the PCM, T_s and T_l denote the temperatures in the solid and liquid regions of the PCM, ρ_s is the density of the solid PCM, L represents the latent heat of the PCM, $s(t)$ is the location of the solidification front (which varies with time t), and T_f is the PCM phase transition temperature.

The concept of rotating fins aims at enhancing heat transfer to overcome the insulating effect of the solid layer. As illustrated in the schematics of Fig. 1(C), rotating fins consist of hollow helical screws rotating around a cylindrical heat transfer surface (e.g. the external surface of a pipe). By rotating, this screw actively scrapes away the solidified PCM layer that forms on the cooling surface. This induces mechanical agitation (obtained by applying a diagonal force with vertical and horizontal components—see Fig. 1(D)) thus favoring thermal homogenization far from the solid surface, due to the movement of the cooled-down solid portion. The dispersion of solid PCM fragments into the liquid promotes multiple nucleation sites as the liquid PCM continues to release heat and solidify. This continuous movement of solid fragments increases the viscosity of the two-phase solid–liquid mixture, thus resulting in a slurry- or mush-like component.

Table 1

Thermo-physical property of Lauric acid ($C_{12}H_{24}O_2$) PCM [32]. s and l refer to solid and liquid phases.

	Lauric acid PCM
Dynamic viscosity, μ [Pa s]	0.00615
Density, ρ [kg/m^3]	867 (l) 1007 (s)
Specific heat capacity, c_p [J/(kg K)]	2030 (s) 2618 (l)
Thermal conductivity, k [W/(m K)]	0.219 (s) 0.142 (l)
Latent heat of fusion, L [kJ/kg]	170.4
Melting temperature, T_{pc} [°C]	45.4
Solidification temperature, T_f [°C]	40.1

3. Materials and methods

3.1. Experiments

A representation of the experimental prototype of the rotating fins PCM battery is shown in Fig. 2(A)–(C), along with its geometrical data (additional details are provided in Supplementary Figure S1). The outer cylindrical shell made of resin has flanged ends designed for connection to the cooling pin fin base. A solid copper pin fin (diameter 10 mm, height 50 mm) with a flanged base was used as the heating and cooling element, mimicking the hollow HTF pipe commonly used in latent thermal energy storage systems. Here, a rotating fin is implemented by a hollow helical aluminum screw with an internal diameter of 11 mm and a nominal external diameter of 25 mm. The clearance between the screw and the copper fin was 0.5 mm, enabling free rotation of the screw while maintaining functional interaction during the experiments. To ensure that phase change occurred exclusively at the copper fin, a 5 mm-thick polyurethane foam insulation, encased in a plastic covering, was applied to the base of the pin fin. A 58 mm-high bronze guide was incorporated to maintain the alignment of the helical screw and facilitate lubrication. Screw rotation was driven by a high-torque (0.3 N m) 12 V DC motor (258-8322, RS Components) operating at 28 RPM.

The thermophysical properties of the considered PCM—lauric acid, a fatty-acid-based organic are summarized in Table 1. Initially, 50 g of pure lauric acid was melted externally in a hot water bath maintained at 65 °C and then gradually poured in a stepwise manner into the cylindrical shell of the experimental device to minimize air bubble entrapment. The PCM was filled to a height approximately 5 mm above the tip of the copper fin to ensure that the fin's free surface remained submerged (see Fig. 2(C)). Four K-type thermocouples (787-7765, RS Components) with uncertainty of ±1.5 °C were inserted at predetermined positions within the PCM (locations detailed in Fig. 2(C)) to monitor the temperature evolution. Three more thermocouples (787-7765, RS Components) are inserted at different height within the copper fin and one additional thermocouples were mounted on the Peltier module surfaces in contact with the copper plate (i.e TC - 8 in Fig. 2(C)).

A schematic representation of the experimental test rig is shown in Fig. 3(A). The TES prototype was placed within a custom-built climatic temperature control chamber constructed from polystyrene foam, featuring a polycarbonate viewing window. The internal chamber temperature was maintained between 38 °C and 44 °C, centered around the PCM solidification point (T_f = 40.1 °C), to prevent premature PCM solidification on the cylinder wall while locating it close to the

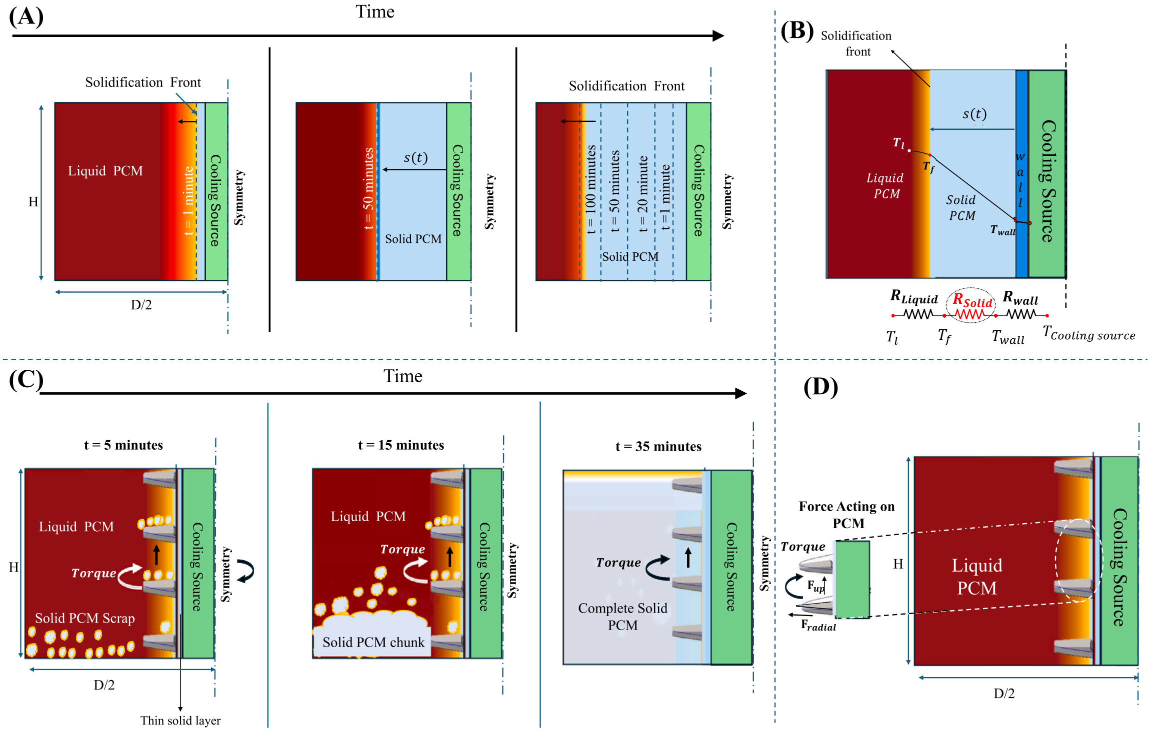

Fig. 1. Comparison between the solidification process in a conventional and a dynamic PCM. (A) Solidification behavior in a conventional PCM-based system, where the solid–liquid interface gradually moves away from the cold surface over time (not in scale). (B) Corresponding temperature profile from the liquid PCM to the cooling source, highlighting that – as solidification progresses – an increasing thickness of the solid PCM layer introduces significant thermal resistance. (C) Solidification mechanism in a rotating fin system, wherein the solidified PCM is detached from the cold surface and displaced into the surrounding liquid PCM, maintaining efficient thermal interaction. (D) Torque-induced force components generated by the rotating screw facilitating PCM detachment and transport away from the heat transfer surface. Dark red indicates melted (liquid) PCM, light blue denotes solidified PCM, and yellow highlights the phase transition region.

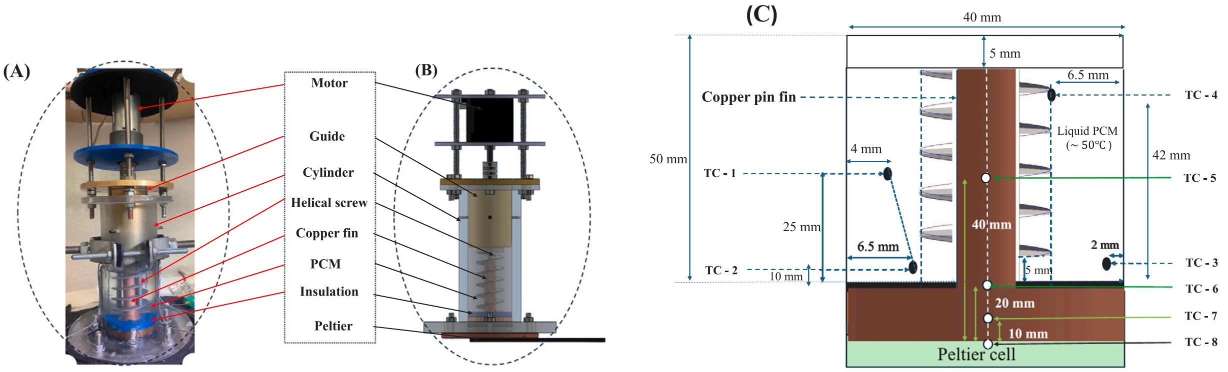

(a) (b)

Fig. 2. Experimental prototype of the rotating fins thermal energy storage: (A) Picture, (B) 3D CAD model, (C) schematics on the location of thermocouples (TC) inside the PCM and in the Solid copper pin fins (reddish-brown color).

copper fin only. This controlled temperature was obtained through a 2300 W hot air gun (187-8995, RS Components), which circulated air into the chamber, with its duty cycle regulated by a thermostat (MTS960) operating under a closed-loop feedback system. Heating and cooling of the copper fin were accomplished via a thermoelectric Peltier module (40 × 40 mm, maximum power 82.1 W; model 490-1373, RS Components). One side of the Peltier was in contact with a copper plate, while the other was attached to a fan-cooled heat sink to dissipate heat during cooling and maintain the hot side at 25 °C. Polarity switching was controlled by an Arduino-based closed-loop system, allowing the hot and cold sides to alternate during heating and cooling cycles.

Both the conventional solidification (baseline) and the solidification with the rotating fin began by melting the solid PCM. The melting was obtained by setting the fin-Peltier interface at a temperature of 60 °C, upon complete melting. This process was just preliminary for the subsequent solidification mechanisms, and therefore was not analyzed in detail. Hence, the discharging of the TES battery (i.e. the PCM solidification) was initiated by lowering the set temperature of TC-8 (see in Fig. 2(C)) to the target cooling temperature. In the static experiment

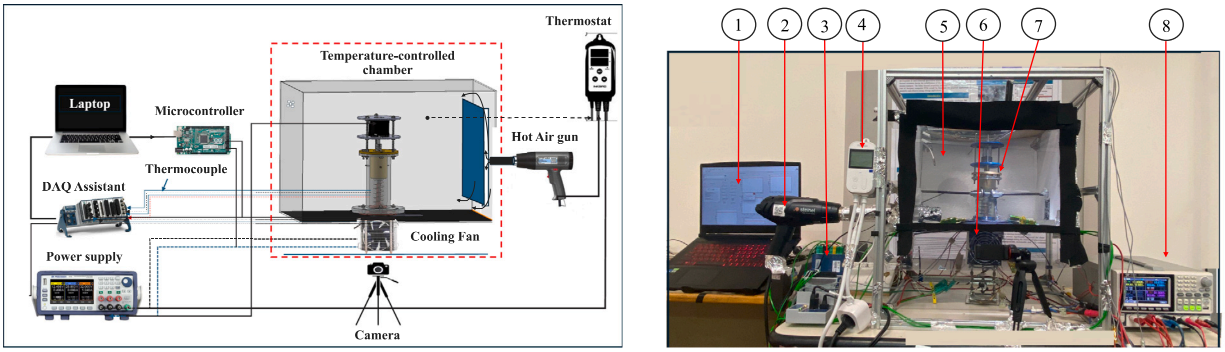

Schematic

(a) Schematic

Implementation

(b) Implementation

Fig. 3. Experimental test rig. **(A)** Schematic of the experimental test rig. **(B)** Implementation of the setup, being: (1) Laptop, (2) hot air gun, (3) DAQ assistant, (4) thermostat, (5) temperature-controlled chamber, (6) fan-cooled heat sink, (7) experimental prototype, (8) power supply.

(conventional solidification), the progression of the solidification front was captured over time using a 2.6 megapixel resolution camera.

In the conventional PCM solidification experiment, the solid fraction over time was obtained from images recorded at 5-minute intervals. Since solid lauric acid PCM is opaque (white), while it is transparent in its liquid phase, a sharp color change occurs at the liquid–solid interface, which can be clearly identified in the recorded images. Accordingly, the solid fraction (solid fraction $= \frac{V_{\text{solid}}}{V_{\text{solid}}+V_{\text{liquid}}}$, where V_{solid} is the solid volume and V_{liquid} is the liquid volume) was determined using a Python-based image analysis library called OpenCV (see Supplementary Figure S4). This method of determining the melting and solid fractions through image analysis is well-established in state-of-the-art PCM visualization studies [49,50]. As pointed out in [51], estimating errors in the determination of the solid and liquid fraction is challenging, as it relies on visual identification with the aid of image analysis tools. For the dynamic experiments, the visual measurements of the solid fraction were not feasible due to the fundamentally different solidification mechanism. Scraped solid PCM chunks from the cooling pipe dispersed throughout the liquid PCM and acted as nucleation sites, forming solid regions throughout the volume. The rotation of the helical fin promotes uniform dispersion of solid PCM fragments within the liquid phase and induces continuous agitation, resulting in a nearly uniform temperature distribution throughout the PCM. Consequently, no significant local hot or cold spots were observed, as it will be confirmed by temperature measurements from thermocouples strategically positioned within the PCM at locations both close to and far from the fin. Therefore, temperature readings from thermocouples placed at various locations were used instead. The thermocouples were evenly distributed outside of the outer circumference of the helical fin (see Fig. 2(C)) to remain stationary during rotation and to capture the spatial and temporal evolution of the PCM temperature field. Hence to accurately identify the end of the solidification process in the dynamic experiments, the solidification completion time was defined as the instant at which the average temperature measured by four thermocouples (TC-1, TC-2, TC-3, and TC-4 in Fig. 2(C)) dropped below the freezing temperature (T_f = 40.1 °C), as determined from DSC measurements.

3.2. Numerical model

3.2.1. Numerical model of the baseline and static cases

Comsol Multiphysics® has been adopted for the numerical simulations of the baseline and static configurations, i.e. the case with bulk PCM and the one with the fin at rest. The computational effort was reduced by adopting simplifying assumptions. A 2D cylindrical section was considered. While it accurately reproduced the baseline case configuration, which is cylindrically symmetrical, this geometry did not account for the inclination of the fins in the static configuration. Nonetheless, this inclination was moderate (approximately 7°) and was therefore not expected to significantly impact the numerical results.

A Dirichlet boundary condition for the temperature was introduced in correspondence with the cooling surfaces, while the bottom small thickness of insulating material was introduced in the lowest horizontal boundary, thus properly reproducing the experimental setup. Insulating heat transfer boundary conditions were imposed at all remaining boundaries. As an initial condition, at time $t = 0$, the PCM was assumed to have a uniform temperature T_{initial}. A schematic picture of those boundary conditions is shown in Figure S3.

The thermal behavior of the PCM in those two configurations was simulated by the enthalpy–porosity method [52]. This approach couples the enthalpy, continuity, and momentum equations to model the thermal behavior of the solid and liquid phases, the phase transition, and the movement of the PCM liquid phase generated by natural convection. The following equations are therefore considered:

$$\rho_{\text{l}} \nabla \cdot \mathbf{v} = 0, \tag{3}$$

$$\rho_{\text{l}} \frac{\partial \mathbf{v}}{\partial t} + \rho_{\text{l}}(\mathbf{v} \cdot \nabla)\mathbf{v} = \nabla \cdot [-p\mathbf{I} + \mathbf{K}] + \mathbf{F}_{\text{g}} + \mathbf{F}_{\text{u}}, \tag{4}$$

$$\rho_{\text{l}} c_{\text{p}}(T) \left(\frac{\partial T}{\partial t} + \mathbf{v} \cdot \nabla T \right) = \nabla \cdot (k(T)\nabla T) + S_{\text{h}}, \tag{5}$$

where

$$\mathbf{K} = \mu(T)(\nabla \mathbf{v} + (\nabla \mathbf{v})^T), \tag{6}$$

$$\mathbf{F}_{\text{u}} = -A(f) \cdot \mathbf{v}, \tag{7}$$

$$\mathbf{F}_{\text{g}} = [\rho_{\text{l}} + \left(\frac{\rho_{\text{l}} - \rho_{\text{s}}}{2\Delta T_m} \right) (T - (T_{\text{pc}} + \Delta T_m))]\mathbf{g}, \tag{8}$$

$$S_{\text{h}} = -\rho_{\text{l}} L \frac{\mathrm{d}f}{\mathrm{d}t}. \tag{9}$$

$\mathbf{F}_{\text{g}}$ is an additional momentum term accounting for the buoyancy effect, where $\mathbf{g}$ is the gravitational acceleration and ΔT_m half of the mushy zone. $\mathbf{F}_{\text{u}}$ is an additional momentum term to include the gradual reduction of the velocity from the liquid value to zero (fully solid PCM) in the mushy zone. According to this approach, the liquid fraction within the mushy zone is treated as fluid flow through a porous medium, where the porosity term $A(f)$ in Eq. (7) is defined based on the Carman–Kozeny relation for porous media flow [53]:

$$A(f) = \frac{\mathrm{C}(1-f)^2}{(f^3 + \epsilon)}. \tag{10}$$

Here, ϵ is a small constant (1e−3) introduced to prevent division by zero during computations, while C is a constant for modeling the structure of the melting front, whose value range from 10^4 to 10^8 [52]. S_h of Eq. (9) is the additional energy term introduced to include the PCM latent heat contribution, as a function of the liquid fraction $f(T)$, whose value is 0 in the fully solid region and 1 in the fully liquid region. Between 0 and 1, its value is generally assumed to vary linearly in the mushy zone, even if more detailed variation curves are emerging from DSC analysis [54]. The thermal conductivity k and specific heat capacity c_p were considered to vary linearly between their solid (subscript s) and liquid (subscript l) values as a function of the temperature:

$$k = k_l + \left(\frac{k_l - k_s}{2\Delta T_m}\right)(T - (T_{pc} + \Delta T_m)), \tag{11}$$

$$c_p = c_{p,l} + \left(\frac{c_{p,l} - c_{p,s}}{2\Delta T_m}\right)(T - (T_{pc} + \Delta T_m)), \tag{12}$$

while the dynamic viscosity μ varied between its liquid value μ_l and a very large value to avoid any movement in the solid phase:

$$\mu = \mu_l(1 + A(f)). \tag{13}$$

To account for errors originating from the input data used in the CFD analysis [55], multiple simulations were conducted with input values varied within a ±5% range from their nominal values [56]. The average temperature values recorded by the sensors were also computed in the numerical simulations to enable direct comparison with experimental data for validation purposes. By computing the baseline and static case, this numerical analysis provides a means to move beyond local temperature measurements and instead assess performance using a global indicator like discharging thermal power. Specifically, the numerical simulations allowed for a comparison of the average thermal power delivered by each configuration up to the point of full discharge, i.e., complete solidification.

3.2.2. Simplified analysis of the dynamic configuration

A comprehensive numerical modeling of the dynamic configuration with rotating fins is challenging due to complexity and the highly multi-physics nature of the phenomena. Fluid flow, heat transfer, phase transition, solid mechanics and fluid–solid interaction physics would be needed in order to properly reproduce the experimental setup. Moreover, a moving mesh would be necessary due to the moving boundaries of the solid and liquid regions. In the context of this study, the aim of the numerical model of the dynamic case was to (i) explore its main working mechanisms, and (ii) define some effective figures of merit related to this novel technique. Hence, towards this end, a simplified approach based on the analytical Neumann solution to the Stefan problem was adopted. According to this analysis, the solidification front evolves with time as:

$$s(t) = 2\lambda\sqrt{\alpha_s t}, \tag{14}$$

where α_s is the thermal diffusivity of the PCM in the solid phase, t is the time, and λ comes from the solution of a proper transcendental equation [57].

The model focuses on the region between two contiguous fins, close to the tube (Fig. 4(A)). Using the experimental rotational speed and pitch of the screw, the vertical velocity of the fins was computed, and the time for a full rotation (t_{round}) was determined (Fig. 4(B)). This corresponds to the time required for the fins to scrape the solidified PCM between initial and final positions.

By simplifying this mechanism, the Stefan solution of the phase transition front in the region between two contiguous fins was considered between time $t = 0$ and t = t_{round}. At time t_{round} the material was imposed to be fully liquid again, and the analysis re-started cyclically in time for every screw rotation. The schematic of this described behavior is displayed in Fig. 4(C). Therefore, this analysis was performed every rotation of the helical screw and was also considered in parallel between all the vertical inter-fins regions. The main simplification of this approach is that the liquid PCM is able to replace the solid PCM that has been scraped instantaneously at t_{round}. This could be a reasonable approach for the first part of the solidification process when the liquid fraction is high, and the overall liquid movement is not hindered. Conversely, the increase in solid fraction progressively hinders the mobility of the remaining liquid phase. To take into account this behavior in the numerical model, the classical formulation given in Eq. (14) was later modified by introducing a penalization term P, as reported in Eq. (15).

$$P = A(f)\frac{C}{\epsilon} \tag{15}$$

This penalization term was computed by scaling between 0 and 1 the porosity term $A(f)$ (shown in Eq. (10)), thus using the same physical background adopted by the enthalpy–porosity method. According to this, when the solid fraction became predominant, the penalization term approaches 0, thus decreasing the computed solidification front $s(t_{round})$ during the specific screw rotation.

The power output predicted by this model represents an idealized estimate of the values expected from experimental measurements, as it simplifies several thermophysical and heat and mass transfer phenomena. Firstly, the model does not account for the thermal resistance present in the clearance between the tube wall and the inner diameter of the helical screw. Secondly, it neglects the temperature reduction caused by heat transfer associated with the forced convection of solid particles induced by the screw's motion. Lastly, the model incorporates all the simplifying assumptions inherent in the one-dimensional Neumann solution to the Stefan problem. Despite these simplifications, the model captures the primary mechanisms of the rotating helical screw fin concept while keeping computational cost low. The resulting performance indicators provide a reasonable basis for preliminary comparison with classical techniques. However, the assumptions may affect the predictions: the solidification front and power density are idealized and may differ from experimental values, particularly at larger scales. Future work could develop a fully coupled multiphysics model to include fluid–structure interaction, moving boundaries, and convective effects in both liquid and solid phases.

4. Results

4.1. Baseline and static fins configurations

4.1.1. Experimental tests

Fig. 5 shows the direct visualization of the solidification process at different times in the baseline configuration. Here, ΔT denotes the temperature difference between the cooling surface and the Freezing point: ΔT of 20 °C and 10 °C where experimentally tested. The temperature profile of the cooling surface is shown in Supplementary Figure S2.

As observed in Fig. 5, the solidification pattern appears fairly symmetrical. Though one might expect that the liquid PCM close to the base of the fin would freeze faster than the portion near the fin tip, the likely reason for the observed symmetry is that the high thermal conductivity of copper facilitates rapid heat transfer from the base to the tip—faster than the rate at which the PCM releases heat due to its low thermal conductivity. The solidification rate is faster for $\Delta T = 20$ °C, as the larger temperature gradient drives higher heat transfer, enabling the PCM to release heat more quickly.

Fig. 6 displays the solid fraction as a function of time for the two temperature differences experimentally tested with the baseline case. The time required for complete solidification at temperature differences of $\Delta T = 20$ °C and $\Delta T = 10$ °C was 75 min and 130 min, respectively.

A performance comparison was conducted using a static fin configuration without any rotation under a temperature difference of $\Delta T = 20$ °C. Fig. 7 presents this comparison in terms of the average PCM temperature during the solidification process. As observed, the static fin configuration enables the PCM to release its latent heat more rapidly

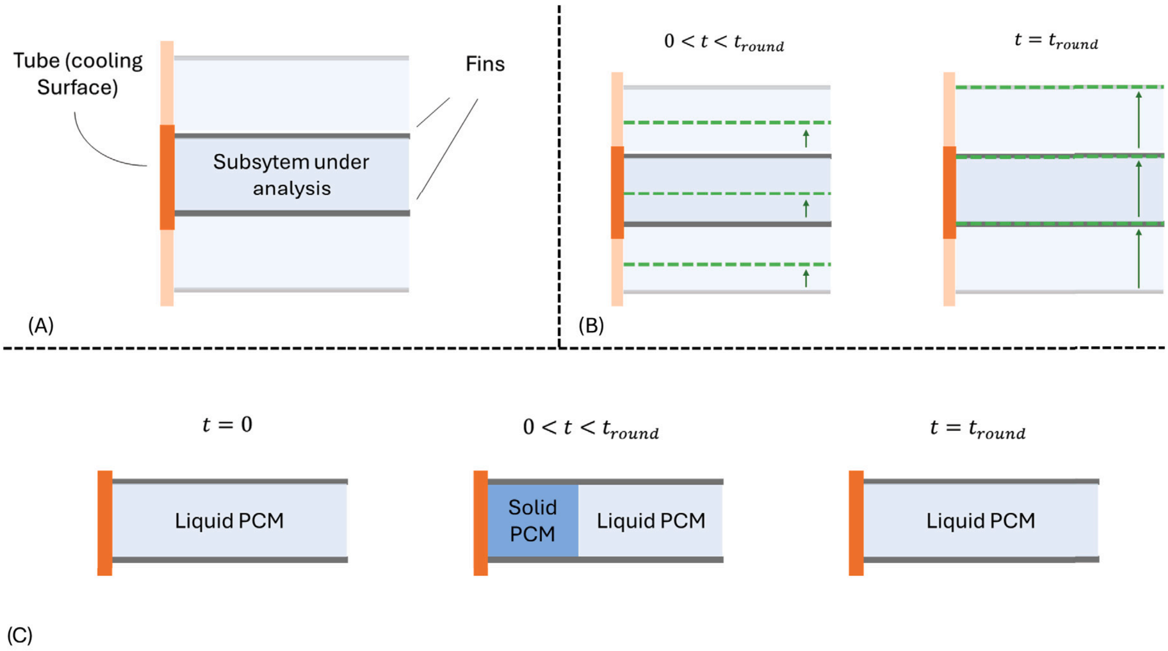

Fig. 4. Schematic of the simplified numerical analysis adopted for the dynamic case. (A) Subsystem under analysis, (B) vertical movement of the fins in the analyzed time frame $0 < t < t_{round}$, (C) and schematic behavior of the solidification process in the considered simplified model.

compared to the baseline case. This enhancement is attributed to the additional heat transfer area provided by the fins, which promotes solidification on their surfaces and facilitates more efficient heat removal. Specifically, when considering the time at which the average PCM temperature crosses the phase transition point ($T_f = 40.1\,°\mathrm{C}$), the static fin configuration demonstrates a 49% improvement, reducing the time required for the PCM to release its latent heat by $\Delta t = 30\,\mathrm{min}$.

4.1.2. *Numerical results*

The main graph (A) of Fig. 8 shows the comparison between the thermal powers released in the two cases during the discharging process, as computed by the CFD simulations. The influence of the static fins is clearly visible during the initial stages of the discharging process, as the static fins power curve (red) reaches higher values with respect to the baseline case. However, the effect of the static fins progressively diminishes, as indicated by the decreasing power trend in the static fin configuration. This reduction occurs because, once a significant layer of solid PCM forms in the region close to the fins, it acts as a thermal insulator, thus vanishing the eventual improvement coming from the insertion of a highly conductive material. The two secondary graphs (B) and (C) of Fig. 8 present the comparisons between the average temperatures recorded by the four sensors (TC-1, TC-2, TC-3 and TC-4 of Fig. 2(C)) as obtained from the numerical model and the experimental tests. Root mean squared errors (RMSE) of 2.03 K and 2.6 K were obtained between the average values of the two curves (represented by the solid lines in Fig. 8(B) and (C)) for the baseline and static configurations, respectively. These results indicate a fair agreement between the numerical model and the experimental data, especially considering that an exact match of local temperatures between the enthalpy–porosity method and the experimental measurements is challenging. That challenge arises from the complexity of accurately reproducing the temperature field, which is influenced by the mechanism of latent heat release or absorption during the phase transition. While this mechanism typically depends on the heat flux applied to the material, the classical enthalpy–porosity method assumes a linear relationship for the release/absorption process. This simplification often results in inaccuracies in capturing the local temperature field, which is crucial for comparison with experimental data obtained through local temperature measurements on the PCM side [54,56].

4.2. *Rotating fins configuration*

4.2.1. *Experimental tests*

Among the primary objectives of this work, we aim at assessing the enhancement of the performance of the discharging process with rotating fins. This enhancement is achieved by lowering the thermal resistance at the heat transfer interface, thereby increasing the system's power density.

Fig. 9 presents the PCM temperature decrease with the screw continuously rotating at 28 RPM, and ΔT of 20 °C and 10 °C. The temperature evolution exhibits a rapid drop during the initial stage, corresponding to sensible cooling in the liquid phase. As the temperature approaches the PCM's solidification point (40.1 °C), the phase change begins, during which latent heat is progressively released upon complete solidification. The temperature data revealed a high degree of uniformity across different thermocouple locations, attributed to the mixing effect induced by the rotating screw. This enhanced mixing minimizes localized cooling, and ensures stable and uniform solidification.

The continuous rotation of the screw also leads to the formation of a mushy, slurry-like PCM structure during the phase transition. Under the given experimental conditions, the latent heat discharge time was 40 and 65 min for temperature differences of $\Delta T = 20\,°\mathrm{C}$ and $\Delta T = 10\,°\mathrm{C}$, respectively.

Fig. 10(A) compares the performance of dynamic PCM solidification at different cooling temperatures with conventional static solidification. In this case, the introduction of the rotating fin led to improvements of 46% and 50% in solidification times for $\Delta T = 20\,°\mathrm{C}$ and $\Delta T = 10\,°\mathrm{C}$, respectively, with respect to the baseline case. Moreover, an experimental investigation was conducted by using intermittent screw rotation instead of continuous rotation as a strategy to optimize the required active external power. A duty cycle of 25% was applied, consisting of 3 min of idle state followed by 1 min of continuous rotation at 28 RPM. The results, illustrated in Fig. 10(B), demonstrate a 37% improvement compared to the baseline case for $\Delta T = 20\,°\mathrm{C}$, with an approximately 10% lower enhancement than the continuous rotation case due to the reduced agitation time, which is limited to short intervals, and the formation of a thin solid layer during idle periods. The application of intermittent rotation requires precise control of the duty cycle. In

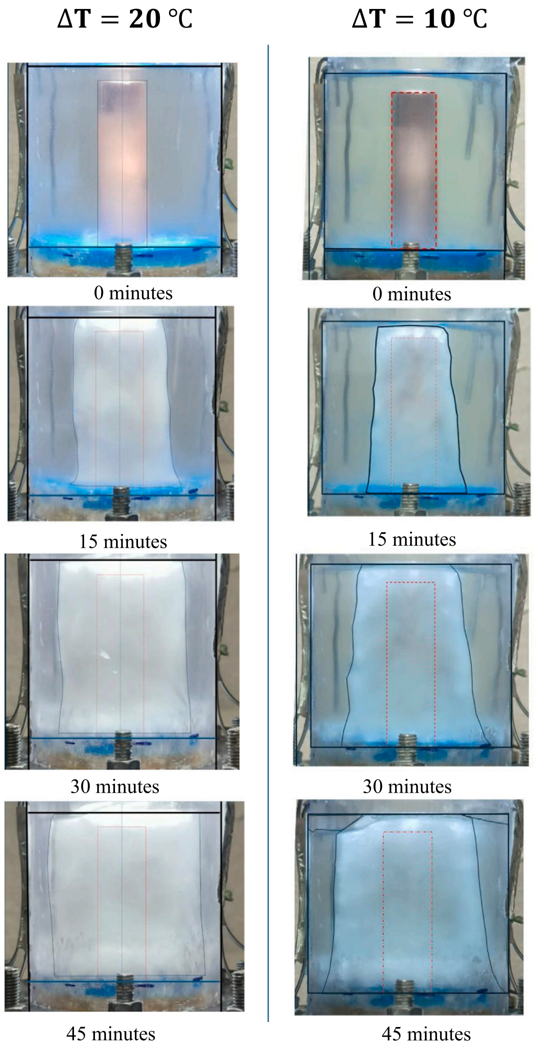

Fig. 5. Experimental pictures of the solidification process at different time snaps in the baseline case. Where ΔT represents the difference between the PCM freezing temperature (T_f) and the cooling temperature of the copper fin, as measured by thermocouple TC-8 (see Fig. 2(C)). The red dashed line highlights the position of the cooling copper fin.

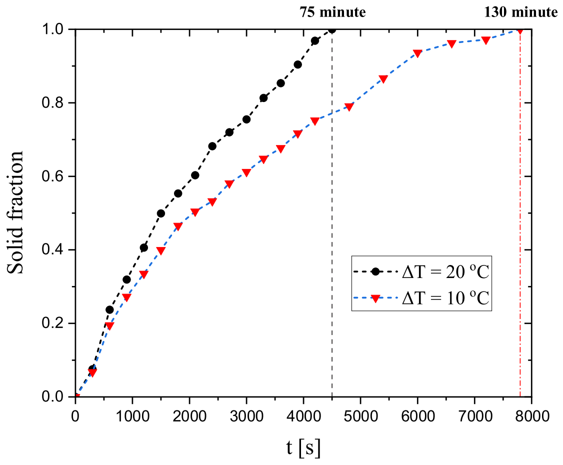

Fig. 6. Temporal evolution of the solid fraction for the baseline cases. The time reported above the graph corresponds to the duration required for the complete release of the stored latent heat.

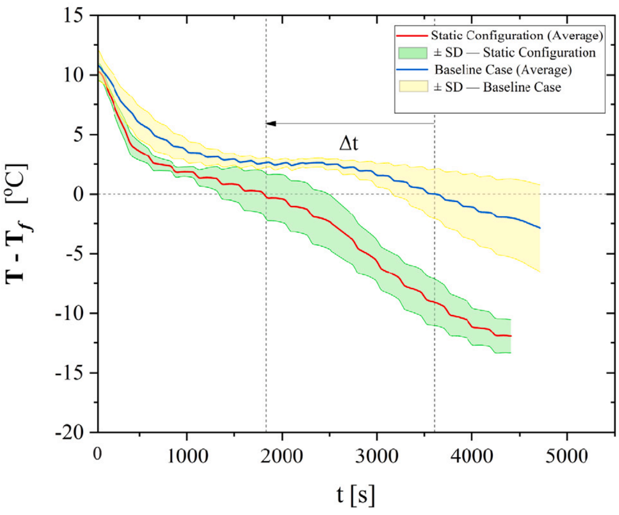

Fig. 7. Average PCM temperature during the solidification under $\Delta T = 20\,^{\circ}\mathrm{C}$, comparing the static fin configuration against the baseline case. Where ΔT represents the difference between the PCM freezing temperature (T_f) and the cooling temperature of the copper fin, as measured by thermocouple TC-8 (see Fig. 2(C)).

particular, reducing the duty cycle increases the idle duration, allowing a subcooled solid PCM layer to progressively accumulate along the cooling pipe. This accumulation results in higher mechanical resistance and requires greater external torque to effectively scrape the solid layer during the subsequent rotation phase. The duty cycle can be optimized based on the imposed temperature difference and the required rate of energy release to meet downstream thermal demand. However, a comprehensive optimization of this operating strategy is left for future study. Hence, future work should focus on systematically optimizing the duty cycle as a function of the cooling temperature difference and solidification rate to achieve an optimal balance between thermal performance and mechanical power requirements.

Quantitatively, for the 50 g of lauric acid used as the phase change material, the mechanical input provided by the continuous motor was 0.88 W, corresponding to a torque of 30 N cm at 28 RPM. This input accounts for approximately 25% of the average thermal power released during the latent heat phase. Despite this relatively modest energy input, the use of mechanical enhancement significantly accelerated the solidification process, reducing system downtime by 46%. As a result, the return on energy investment reached 1.9×, thereby improving process throughput and offering potential reductions in operational costs. Future work will focus on optimizing the rotation speed and system design to maximize this energy benefit.

4.2.2. *Numerical results*

Fig. 11 presents the comparison between the average power predicted by the simplified numerical approach and the values obtained from CFD simulations for both the static and baseline cases. The results highlight the outstanding performance of the numerical model, which serves as an ideal upper limit to the experimentally tested dynamic configuration, owing to the simplifying assumptions described earlier.

The rotational speed of the novel helical screw remarkably affects the performance of the proposed solution. A higher rotational velocity led to a lower t_{round} and a higher power, as the self-insulating behavior of the solid PCM layer is avoided by a faster scraping. Therefore, a sensitivity analysis of the power with respect to the rotational speed have been performed by means of the numerical model, in order to assess the ideal power curves at the different speeds. The power and energy curves plotted against the solidification time for rotational speeds between 1 and 100 RPM are plotted in Fig. 12(A) and (B),

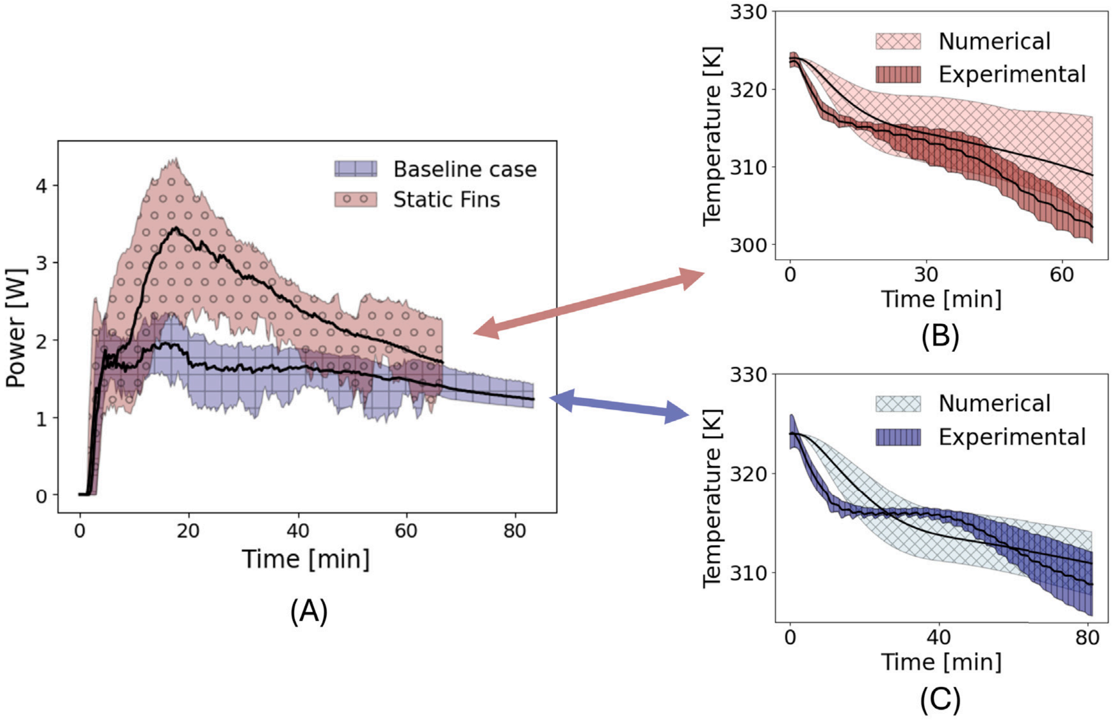

Fig. 8. Comparison of the released thermal power as a function of time of the baseline and static cases obtained through numerical simulations (A). The onset graphs represent the validations of the numerical models against experimental results for the static (B) and baseline (C) cases. The error bars shown for the numerical models–covering both curves in (A) as well as the numerical curves in (B) and (C)–represent a variation of ±5% in the input values, as detailed in the methodology section.

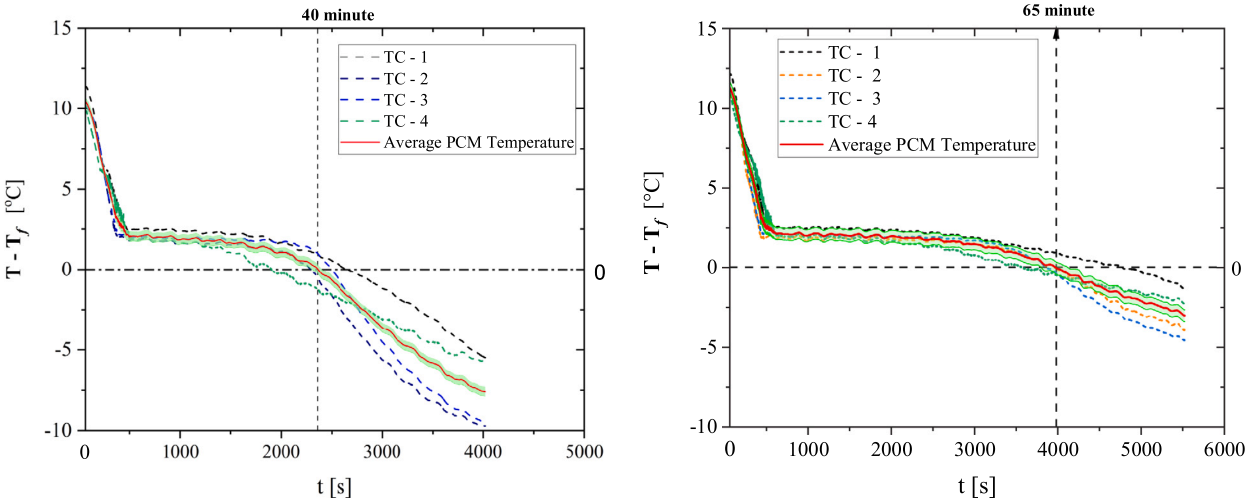

(a) ΔT = 20 °C.

(b) ΔT = 10 °C.

Fig. 9. PCM temperature evolution at different thermocouple locations under dynamic conditions, with the screw rotating continuously at 28 RPM. The copper fin is cooled at a temperature difference of (**A**) $\Delta T = 20$ °C, where complete latent heat release is achieved at 40 min, and (**B**) $\Delta T = 10$ °C, where complete latent heat release occurs at 65 min, relative to the PCM solidification temperature ($T_f = 40.1$ °C). The *y*-axis represents the PCM temperature normalized relative to the freezing point in order to highlight the thermal driving potential and clearly indicate the point of complete latent heat extraction. The experimental uncertainty is depicted by the green bands.

respectively. A maximum power of almost 40 W was reached with a rotational speed of 100 RPM. As illustrated by the energy curves on Fig. 12(B), the benefits of increasing rotational speed on power enhancement diminish, especially at higher RPM values. Thus, for each specific application, an optimal range of rotational speed should be identified to achieve the desired solidification rate while minimizing RPM—and thereby reducing the power demand of the rotating system. It is worth also noting that the decreasing trend of each power curve as a function of the time is due to the penalization term P shown in Eq. (15), which is imposed to simulate the difficulty for the PCM liquid to reach the neighboring tubes attributed to the presence of a slurry-like material (as the solid fraction of PCM becomes relevant). Finally, it

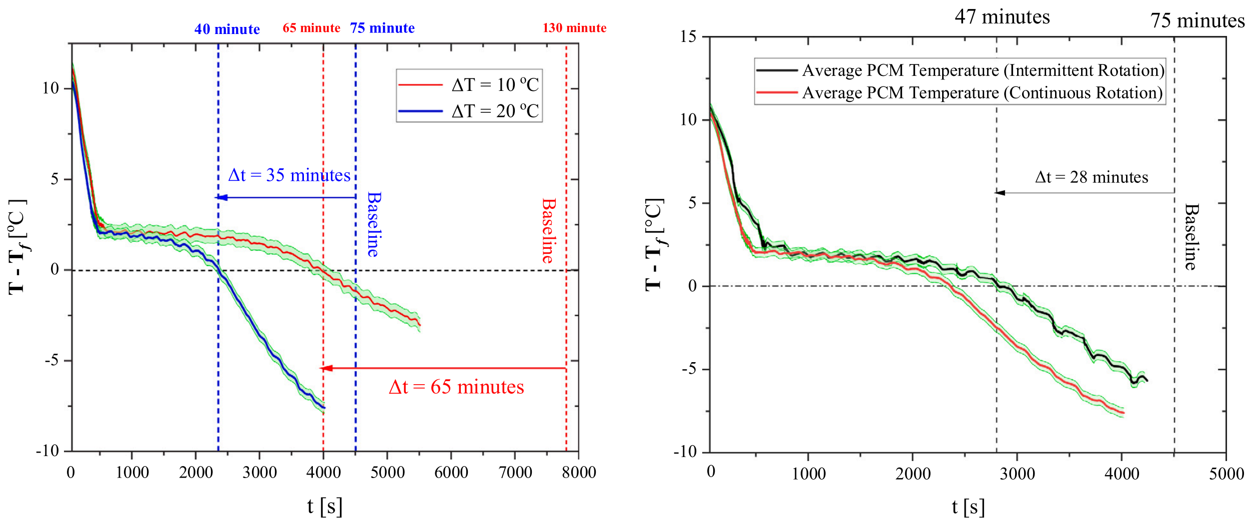

(a) Continuous rotation

(b) Intermittent Motor operation (Duty cycle =25%)

Fig. 10. **(A)** Comparison of discharge times between conventional (Baseline) and dynamic PCM configurations, based on the average PCM temperature evolution, with cooling loads corresponding to temperature differentials of $\Delta T = 20\,^\circ\mathrm{C}$ and $\Delta T = 30\,^\circ\mathrm{C}$ relative to the PCM solidification temperature (T_f) from the Copper fin temperature as measured by TC- 8. The vertical dashed lines indicate the time required for complete latent heat release: blue lines correspond to $\Delta T = 20\,^\circ\mathrm{C}$ and red lines to $\Delta T = 30\,^\circ\mathrm{C}$, for both configurations. The dynamic PCM configuration demonstrates a marked reduction in discharge time—35 min for $\Delta T = 20\,^\circ\mathrm{C}$ and 65 min for $\Delta T = 30\,^\circ\mathrm{C}$, indicating significantly improved latent heat extraction and thermal response compared to the conventional PCM (Baseline). The experimental uncertainty is depicted by the green bands. **(B)** Comparative analysis with Baseline (conventional PCM), Intermittent Rotation (Duty cycle = 25%) and Continuous Rotation for $\Delta T = 20\,^\circ\mathrm{C}$.

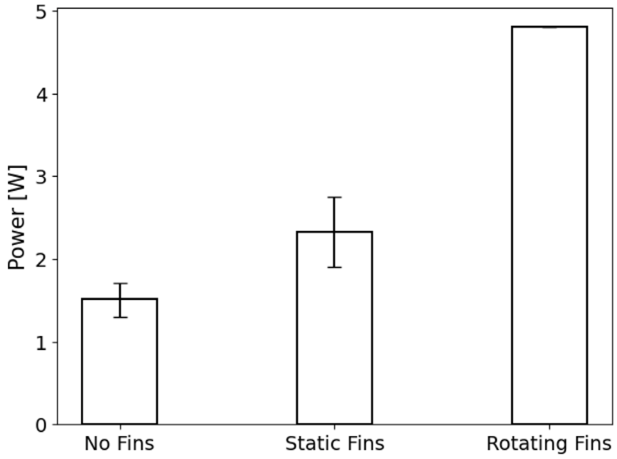

Fig. 11. Mean power comparison between the baseline, static, and rotating configurations estimated by the numerical models at 28 rpm with continuous rotation.

should be noted that the simplified model described here considers only the phase transition behavior and neglects the sensible contributions of both the solid and liquid phases, thus being an ideal upper limit of the power and energy trends. Clearly, such a discrepancy is case specific and shall be estimated depending on the design of individual thermal batteries.

5. Conclusions

A proof of concept for dynamically enhancing the power density of latent thermal energy storage has been proposed and tested in this work. The studied system consists of hollow rotating fins which can be fitted around a cylindrical surface of a pipe where heat is transferred to and/or from a PCM. In the latter configuration, referred to as rotating fins in PCMs (RotFinPCM), the scraping action of the screw at the heat transfer interface dramatically reduces the detrimental thermal resistance of standard latent batteries with a reduction in discharging and charging times. To our best knowledge, unlike other recent attempts in the literature based on rotating mechanical elements (e.g. [43]), the RotFinPCM appears more suitable for retrofitting existing complex heat exchangers based on tube arrays such as the popular shell and tube configurations. Importantly, although the present study has been focused on the solidification phase (as this is recognized to be the bottleneck for the increase of power density in latent thermal energy storage applications [48]) the concept is intrinsically reversible and can thus be adopted also for enhancing the melting phase in future works. The latter aspect makes RotFinPCM suitable for cyclable thermal batteries.

From an application perspective, the proposed solution is most relevant for PCM-based thermal energy storage systems in which power density, rather than energy density, limits overall performance. Potential application areas include compact thermal buffers for waste heat recovery, thermal management of high-power electronic or electrochemical systems, and medium-scale thermal batteries for load shifting and peak shaving. Furthermore, RotFinPCM is particularly promising for applications involving nano-enhanced composite PCMs, where the screw-induced mixing can improve nanoparticle dispersion, thus mitigating sedimentation during solidification, which is known to be one of the key challenges in nano-enhanced PCM applications [32]. Like all concepts that rely on moving mechanical components, the RotFinPCM system requires an external mechanical power source, which results in additional energy consumption. The introduction of rotating elements also increases the overall complexity of the TES unit, potentially leading to higher maintenance requirements and a greater risk of mechanical failure. Additional critical aspects include sealing and leakage risks at rotating interfaces, material durability under combined thermal cycling and mechanical stress, the need to verify a positive net energy benefit when auxiliary power is considered, increased control-system complexity, possible noise and vibration, and cost and manufacturability constraints at larger scale. These limitations should be systematically evaluated through dedicated experimental campaigns

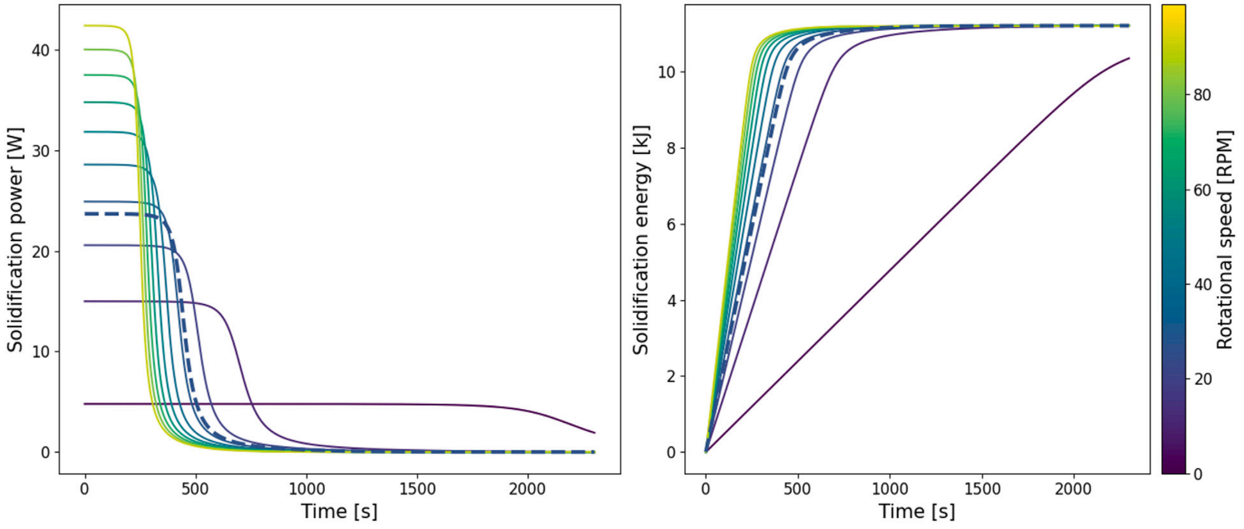

(A) (B)

Fig. 12. Sensitivity analysis of the discharging power (A) and energy (B) curves as a function of the screw rotational speed and solidification time. The scattered lines represent the rotational speed experimentally tested in this study (28 RPM).

to assess the long-term feasibility, reliability, and scalability of the technology.

The present work is therefore intended as a laboratory-scale proof of concept aimed at demonstrating the feasibility and effectiveness of a combined scraping and mixing mechanism for enhancing heat transfer in latent thermal energy storage. Future research will focus on long-term cycling tests, optimization of rotational speed and geometry, evaluation of mechanical power consumption, and techno-economic assessments to fully assess the reliability, scalability, and practical viability of the RotFinPCM concept.

CRediT authorship contribution statement

Biruk Agegnehu: Writing – original draft, Visualization, Validation, Methodology, Investigation, Formal analysis, Data curation. **Alessandro Ribezzo:** Writing – review & editing, Visualization, Validation, Software, Methodology, Investigation, Formal analysis, Data curation. **Andrea Bottega:** Writing – review & editing, Supervision, Methodology. **Matteo Morciano:** Writing – review & editing, Supervision, Software, Methodology, Investigation, Formal analysis, Data curation. **Matteo Fasano:** Writing – review & editing, Supervision, Methodology, Formal analysis, Data curation, Conceptualization. **Eliodoro Chiavazzo:** Writing – review & editing, Supervision, Resources, Project administration, Funding acquisition, Conceptualization.

Declaration of competing interest

The authors declare the following financial interests/personal relationships which may be considered as potential competing interests: Eliodoro Chiavazzo reports financial support was provided by Ministry of Education and Merit. If there are other authors, they declare that they have no known competing financial interests or personal relationships that could have appeared to influence the work reported in this paper.

Acknowledgments

The authors wish to gratefully acknowledge useful discussions with Dr. Amit Kumar Mishra. E.C. acknowledges partial funding under the National Recovery and Resilience Plan (PNRR), Mission 4 Component 2 Investment 1.3-Call for tender No. 1561 of 11.10.2022 of Ministero dell'Università e della Ricerca (MUR), funded by the European Union NextGenerationEU. E.C. acknowledges partial support by Ministero dell'Ambiente e della Sicurezza Energetica (MASE) and ENEA under the research contract PTR 2025-2027.

Appendix A. Supplementary data

Supplementary material related to this article can be found online at https://doi.org/10.1016/j.est.2026.121877.

Data availability

Data will be made available on request.

References

[1] S.F. Ahmed, N. Rafa, T. Mehnaz, B. Ahmed, N. Islam, M. Mofijur, A.T. Hoang, G. Shafiullah, Integration of phase change materials in improving the performance of heating, cooling, and clean energy storage systems: An overview, J. Clean. Prod. 364 (2022) 132639.

[2] G. Hekimoğlu, A. Sarı, A review on phase change materials (PCMs) for thermal energy storage implementations, Mater. Today: Proc. 58 (2022) 1360–1367.

[3] R. Kandasamy, X.-Q. Wang, A.S. Mujumdar, Application of phase change materials in thermal management of electronics, Appl. Therm. Eng. 27 (2007) 2822–2832.

[4] A. Arshad, H.M. Ali, S. Khushnood, M. Jabbal, Experimental investigation of PCM based round pin-fin heat sinks for thermal management of electronics: effect of pin-fin diameter, Int. J. Heat Mass Transfer 117 (2018) 861–872.

[5] N. Sarier, E. Onder, Organic phase change materials and their textile applications: an overview, Thermochim. Acta 540 (2012) 7–60.

[6] M. Izadi, S.F. Taghavi, S.H.N. Safavi, F. Afsharpanah, W. Yaïci, Thermal management of shelter building walls by PCM macro-encapsulation in commercial hollow bricks, Case Stud. Therm. Eng. 47 (2023) 103081.

[7] A. Anand, M. Mansor, K. Sharma, A. Shukla, A. Sharma, M.I.H. Siddiqui, K.K. Sadasivuni, N. Priyadarshi, B. Twala, A comprehensive review on eutectic phase change materials: Development, thermophysical properties, thermal stability, reliability, and applications, Alex. Eng. J. 112 (2025) 254–280.

[8] T. Yang, W.P. King, N. Miljkovic, Phase change material-based thermal energy storage, Cell Rep. Phys. Sci. 2 (2021).

[9] A. Ribezzo, G. Falciani, L. Bergamasco, M. Fasano, E. Chiavazzo, An overview on the use of additives and preparation procedure in phase change materials for thermal energy storage with a focus on long term applications, J. Energy Storage 53 (2022) 105140.

[10] A.H. Al-Mudhafar, A.F. Nowakowski, F.C. Nicolleau, Enhancing the thermal performance of PCM in a shell and tube latent heat energy storage system by utilizing innovative fins, Energy Rep. 7 (2021) 120–126.

[11] M. Morciano, M. Alberghini, M. Fasano, M. Almiento, F. Calignano, D. Manfredi, P. Asinari, E. Chiavazzo, 3D printed lattice metal structures for enhanced heat transfer in latent heat storage systems, J. Energy Storage 65 (2023) 107350.

[12] A. Ribezzo, M. Morciano, G. Zsembinszki, S.R. Amigó, S.M. Kala, E. Borri, L. Bergamasco, M. Fasano, E. Chiavazzo, C. Prieto, et al., Enhancement of heat transfer through the incorporation of copper metal wool in latent heat thermal energy storage systems, Renew. Energy 231 (2024) 120888.

[13] S.L. Tariq, H.M. Ali, M.A. Akram, M.M. Janjua, M. Ahmadlouydarab, Nanoparticles enhanced phase change materials (NePCMs)-A recent review, Appl. Therm. Eng. 176 (2020) 115305.

[14] Z. Said, H. Zeyad, T.I. Eisa, M.E.H. Assad, Nano-enhanced PCM for energy storage, in: 2019 Advances in Science and Engineering Technology International Conferences, ASET, IEEE, 2019, pp. 1–6.

[15] S. Shoeibi, F. Jamil, S.M. Parsa, S. Mehdi, H. Kargarsharifabad, S.A.A. Mirjalily, W. Guo, H.H. Ngo, B.-J. Ni, M. Khiadani, Recent advancements in applications of encapsulated phase change materials for solar energy systems: A state of the art review, J. Energy Storage 94 (2024) 112401.

[16] S.A. Albdour, Z. Haddad, O.Z. Sharaf, A. Alazzam, E. Abu-Nada, Micro/nano-encapsulated phase-change materials (ePCMs) for solar photothermal absorption and storage: Fundamentals, recent advances, and future directions, Prog. Energy Combust. Sci. 93 (2022) 101037.

[17] B.M. Diaconu, M. Cruceru, L. Anghelescu, A critical review on heat transfer enhancement techniques in latent heat storage systems based on phase change materials. Passive and active techniques, system designs and optimization, J. Energy Storage 61 (2023) 106830.

[18] A.K. Mishra, A. Ribezzo, M. Morciano, L. Bergamasco, E. Campagnoli, V. Giaretto, M. Fasano, E. Chiavazzo, Thermal conductivity enhancement in carbon black composite pcm for thermal energy storage, J. Phys.: Conf. Ser. 2940 (2025) 012012.

[19] G. Wu, S. Chen, S. Zeng, Effects of mechanical vibration on melting behaviour of phase change material during charging process, Appl. Therm. Eng. 192 (2021) 116914.

[20] Y. Wu, M. Luo, S. Chen, W. Zhou, Y. Yu, Z. Zhou, Numerical simulation study of the effect of mechanical vibration on heat transfer in a six-fin latent heat thermal energy storage unit, Int. J. Heat Mass Transfer 207 (2023) 123996.

[21] W. Zhang, X. Li, W. Wu, J. Huang, Influence of mechanical vibration on composite phase change material based thermal management system for lithium-ion battery, J. Energy Storage 54 (2022) 105237.

[22] S.H. Choi, J. Park, H.S. Ko, S.W. Karng, Heat penetration reduction through PCM walls via bubble injections in buildings, Energy Convers. Manage. 221 (2020) 113187.

[23] S. Yang, X.-F. Shao, H.-Y. Shi, J.-H. Luo, L.-W. Fan, Bubble-injection-enabled significant reduction of supercooling and controllable triggering of crystallization of erythritol for medium-temperature thermal energy storage, Sol. Energy Mater. Sol. Cells 236 (2022) 111538.

[24] Sung Ho Choi, Han Seo Ko, Dong Kee Sohn, Bubble-driven flow enhancement of heat discharge of latent heat thermal energy storage, Energy 244 (2022) 123168.

[25] S.H. Choi, D.K. Sohn, H.S. Ko, Performance enhancement of latent heat thermal energy storage by bubble-driven flow, Appl. Energy 302 (2021) 117520.

[26] M. Xing, D. Jing, H. Chen, H. Zhang, R. Wang, Ice thermal energy storage enhancement using aligned carbon nanotubes under external magnetic field, J. Energy Storage 56 (2022) 105931.

[27] D. Nakhla, J.S. Cotton, Effect of electrohydrodynamic (EHD) forces on charging of a vertical latent heat thermal storage module filled with octadecane, Int. J. Heat Mass Transfer 167 (2021) 120828.

[28] H. Daghooghi-Mobarakeh, V. Subramanian, P.E. Phelan, Experimental study of water freezing process improvement using ultrasound, Appl. Therm. Eng. 202 (2022) 117827.

[29] F. Selimefendigil, H.F. Öztop, Mixed convection in a PCM filled cavity under the influence of a rotating cylinder, Sol. Energy 200 (2020) 61–75.

[30] W. Fu, X. Yan, Y. Gurumukhi, V.S. Garimella, W.P. King, N. Miljkovic, High power and energy density dynamic phase change materials using pressure-enhanced close contact melting, Nat. Energy 7 (2022) 270–280.

[31] B. Agegnehu, K. Liebezeit, M. Fasano, M. Morciano, E. Chiavazzo, Dynamic PCM for high-performance latent thermal energy storage: A numerical and parametric study, Int. Commun. Heat Mass Transfer 167 (2025) 109277.

[32] A.K. Mishra, M. Morciano, B.W. Agegnehu, E. Campagnoli, V. Giaretto, A. Bottega, M. Fasano, L. Mongibello, E. Chiavazzo, Dynamic PCM strategies with nano-enhanced composites for optimal thermal energy storage and management, Chem. Eng. J. Adv. (2025) 100789.

[33] K. Shank, S. Tiari, A review on active heat transfer enhancement techniques within latent heat thermal energy storage systems, Energies 16 (2023) 4165.

[34] X. Huang, F. Li, T. Xiao, J. Guo, F. Wang, X. Gao, X. Yang, Y.-L. He, Investigation and optimization of solidification performance of a triplex-tube latent heat thermal energy storage system by rotational mechanism, Appl. Energy 331 (2023) 120435.

[35] H. Soltani, M. Soltani, H. Karimi, J. Nathwani, Heat transfer enhancement in latent heat thermal energy storage unit using a combination of fins and rotational mechanisms, Int. J. Heat Mass Transfer 179 (2021) 121667.

[36] H. Soltani, M. Soltani, H. Karimi, J. Nathwani, Optimization of shell and tube thermal energy storage unit based on the effects of adding fins, nanoparticles and rotational mechanism, J. Clean. Prod. 331 (2022) 129922.

[37] X. Yu, R. Jiang, Z. Li, G. Qian, B. Wang, L. Wang, R. Huang, Synergistic improvement of melting rate and heat storage capacity by a rotation-based method for shell-and-tube latent thermal energy storage, Appl. Therm. Eng. 219 (2023) 119480.

[38] A.J. Khosroshahi, S. Hossainpour, Investigation of storage rotation effect on phase change material charging process in latent heat thermal energy storage system, J. Energy Storage 36 (2021) 102442.

[39] S. Hossainpour, et al., A numerical investigation on the finned storage rotation effect on the phase change material melting process of latent heat thermal energy storage system, J. Energy Storage 55 (2022) 105461.

[40] M.I. Fathi, M.A. Mussa, Experimental study on the effect of tube rotation on performance of horizontal shell and tube latent heat energy storage, J. Energy Storage 39 (2021) 102626.

[41] C. Yang, Z.-J. Zheng, X. Cai, Y. Xu, Experimental study on the effect of rotation on melting performance of shell-and-tube latent heat thermal energy storage unit, Appl. Therm. Eng. 215 (2022) 118877.

[42] F. Essa, A. Abdullah, W.H. Alawee, A. Alarjani, U.F. Alqsair, S. Shanmugan, Z. Omara, M. Younes, Experimental enhancement of tubular solar still performance using rotating cylinder, nanoparticles' coating, parabolic solar concentrator, and phase change material, Case Stud. Therm. Eng. 29 (2022) 101705.

[43] N. Maruoka, T. Tsutsumi, A. Ito, M. Hayasaka, H. Nogami, Heat release characteristics of a latent heat storage heat exchanger by scraping the solidified phase change material layer, Energy 205 (2020) 118055.

[44] A. Egea, A. García, R. Herrero-Martín, J. Pérez-García, Experimental performance of a novel scraped surface heat exchanger for latent energy storage for domestic hot water generation, Renew. Energy 193 (2022) 870–878.

[45] J. Tombrink, H. Jockenhöfer, D. Bauer, Experimental investigation of a rotating drum heat exchanger for latent heat storage, Appl. Therm. Eng. 183 (2021) 116221.

[46] J. Tombrink, D. Bauer, Simulation of a rotating drum heat exchanger for latent heat storage using a quasistationary analytical approach and a numerical transient finite difference scheme, Appl. Therm. Eng. 194 (2021) 117029.

[47] J. Tombrink, D. Bauer, Demand-based process steam from renewable energy: Implementation and sizing of a latent heat thermal energy storage system based on the Rotating Drum Heat Exchanger, Appl. Energy 321 (2022) 119325.

[48] A. Ribezzo, L. Bergamasco, M. Morciano, M. Fasano, L. Mongibello, E. Chiavazzo, Experimental analysis of carbon-based phase change materials composites for a fast numerical design of cold energy storage systems, Appl. Therm. Eng. 231 (2023) 120907.

[49] A. Majumadar, T. Niphadkar, et al., An image processing algorithm to estimate the melt fraction and energy storage of a PCM enclosed in a spherical capsule, Int. J. Energy Res. 43 (2019).

[50] K.P. Shete, I. Dujovne, S.M. de Bruyn Kops, D.B. Kosanovic, Creating dimensionless performance curves for latent heat thermal energy storage, Int. J. Heat Mass Transfer 236 (2025) 126225.

[51] I. Salman, T. Shockner, R.A. Stavins, S. Kim, E. Koronio, O. Gal, M.S. Spector, W.P. King, N. Miljkovic, G. Ziskind, A "hourglass" system for transient thermal management based on dynamic close-contact melting of a phase-change material, Int. J. Heat Mass Transfer 239 (2025) 126542.

[52] A. Martínez, M. Carmona, C. Cortés, I. Arauzo, Experimentally based testing of the enthalpy-porosity method for the numerical simulation of phase change of paraffin-type pcms, J. Energy Storage 69 (2023) 107876.

[53] B. Niezgoda-Żelasko, The enthalpy-porosity method applied to the modelling of the ice slurry melting process during tube flow, Procedia Eng. 157 (2016) 114–121.

[54] M. Goderis, A. Buruzs, F. Giordano, T. Barz, W. Beyne, M. De Paepe, Numerical modelling of thermal hysteresis in melting and solidification of phase change materials, J. Phys.: Conf. Ser. 2766 (2024) 012227.

[55] A. Stamatiou, S. Maranda, L.J. Fischer, J. Worlitschek, Solid–Liquid Phase Change Materials for Energy Storage, CRC Press, 2022, pp. 15–36, http://dx.doi.org/10.1201/9781003213260-2.

[56] A. Ribezzo, M. Morciano, G. Zsembinszki, S.M. Kala, E. Borri, L. Bergamasco, M. Fasano, E. Chiavazzo, C. Prieto, L.F. Cabeza, Numerical analysis of an optimal metal wool-phase change material for thermal energy storage with exceptionally high power density, Appl. Therm. Eng. 273 (2025) 126429.

[57] D.W. Hahn, M.N. Özişik, Frontmatter, John Wiley and Sons, Inc. 2012, pp. i–xxx, http://dx.doi.org/10.1002/9781118411285.fmatter.